Luminescence from β-$FeSi_2$ precipitates in Si. I. Morphology and epitaxial relationship

M. G. Grimaldi
INFM and Dipartimento di Fisica, Università di Catania, Corso Italia 57, 95129 Catania, Italy

C. Bongiorno and C. Spinella
CNR-IMM, Stradale Primosole 50, 95127 Catania, Italy

E. Grilli, L. Martinelli, M. Gemelli, D. B. Migas, and Leo Miglio
INFM and Dipartimento di Scienza dei Materiali, Università degli studi di Milano-Bicocca, via Cozzi 53, 20125 Milano, Italy

M. Fanciulli
Laboratorio MDM-INFM, via Olivetti 2, 20041 Agrate Brianza (MI), Italy
(Received 29 October 2001; published 21 August 2002)

The goal of this paper is to investigate the morphology and the structure of ion-beam synthesized β-$FeSi_2$ precipitates and the defects in the Si matrix by using transmission electron microscopy (TEM) and, in a few cases, conversion electron Mössbauer spectroscopy or Rutherford backscattering spectrometry. We shall point out how the different process parameters affect the resulting structure and the optimum process window for light emitting application of β-$FeSi_2$. In particular, we will also show that within the optimum process window at least two different types of precipitates are obtained in separate regions: small ball-shaped precipitates in the surface region and large disc-shaped precipitates deeper in the sample. The latter are shown to display a very good interface to the Si matrix, as obtained by TEM analysis and dedicated molecular dynamics simulation. In the second part of this paper [Martinelli *et al.*, Phys. Rev. B **66**, 085320 (2002)], the nature and the origin of the 1.54-μm photoluminescence signal obtained from our best samples will be analyzed in detail.

DOI: 10.1103/PhysRevB.66.085319 PACS number(s): 68.35.Dv, 61.72.Tt, 81.40.Ef

I. INTRODUCTION

In the past 20 years, semiconducting β-$FeSi_2$ has continued to attract attention due to its potential applications for silicon-based optoelectronic components.[1] Optical measurements of the absorption edge on continuous β-$FeSi_2$ films in and on Si have indicated a very promising energy gap of ~ 0.85 eV (~ 1.5 μm), still the data analysis did not allow a definitive indication whether the fundamental gap is direct or not (for a recent review, see Ref. 2). *Ab initio* band-structure calculations for the base-centered orthorhombic cell with lattice constants $a=9.86$ Å, $b=7.79$ Å, and $c=7.83$ Å predicted a direct gap of 0.6–0.8 eV, and an indirect transition some tens of meV lower in energy.[3–9] In connection with the epitaxial relationship with the silicon matrix, one additional issue to be taken into account is the strain: in fact, some *ab initio* calculations have recently pointed out that the gap shape of β-$FeSi_2$ does depend on strain, even if the nature is likely to remain indirect.[6–8] A weak photoluminescence (PL) signal from continuous β-$FeSi_2$ film was only observed at 5 K, despite the high quality of the crystalline material, still the origin was not clear.[1] It seemed, therefore, that β-$FeSi_2$ was an unsuitable candidate for light emitting applications. However, the recent observation of room temperature electroluminescence signal at about 1.6 μm from ion-beam (IBS) synthesized[10] and molecular beam epitaxy (MBE) grown[11] β-$FeSi_2$ microcrystals in Si has drastically renewed the interest of the scientific community in this material. In the former case, a Si wafer was previously implanted with Fe ions at high current and at doses between 1×10^{15} and 1×10^{17} cm^{-2}, then annealed at 900 °C, and precipitates are formed. During implantation the substrate temperature rose to 500 °C because of the beam heating, so that amorphization of the Si substrate was avoided. The resulting structure contained β-$FeSi_2$ precipitates of 40–60 nm in size, embedded in a highly defective region of silicon just below the surface, and a dislocation network at a depth corresponding to the end of range of the implant.[12,13]

In order to get a better understanding of the origin of the 1.54 μm light emission from iron-implanted Si, a few critical issues, concerning the evolution of defects and precipitates with processing parameters as well as the correlation between structural and optical properties, require further complementary investigations. Moreover, in a recent paper[13] it has been shown that only one type of precipitates (disk-shaped, with the diameter of 100–200 nm and the thickness of 20–30 nm) exhibits PL signal.

Both morphology and structure of ion-beam synthesized precipitates depend, in a complex way, on several parameters, such as the implantation temperature, flux and fluence, and the annealing temperature. The effect of these parameters on defect evolution must be taken into account in order to optimize the process for light emission applications. Moreover, the defect distribution may affect the size and concentration profile of the precipitates. In fact, defects may act as nucleation centers for precipitation and silicide precipitates may be a sink of interstitial silicon, because of a smaller volume per atom in β-$FeSi_2$ (12.5 $Å^3$) with respect to the one in pure Si (20.01 $Å^3$) (for details see Sec. III A).

It is known that β-$FeSi_2$ appears in two stable phases: nonstoichiometric (Fe deficient) tetragonal metallic α phase

($a=2.695$ Å and $c=5.390$ Å), stable at temperature above $\sim 950\,^{\circ}$C, and orthorhombic semiconducting β phase, stable at lower temperatures.[14] The existence of two metallic metastable phases, not present in the bulk phase diagram, having the fluorite structure (γ-$FeSi_2$, $a=5.389$ Å) and the CsCl-defective structure ($a=2.7$ Å), respectively, has been observed in ultrathin epilayers on a Si substrate[15–17] or small coherent precipitates in a Si matrix[18–20]. The α phase is better lattice matched with Si than the β phase for symmetry reasons, and the cubic γ phase also has the smallest lattice mismatch to Si among the three $FeSi_2$ phases. In small coherent $FeSi_2$ precipitates the α and γ phases have been shown by many authors to be stabilized by the epitaxy with the Si matrix,[15–17] as long as the interface energy dominates over the volume energy. Therefore, the phase formed in nanometric precipitates cannot be simply predicted on the basis of the bulk phase diagram.

The goal of this paper is to investigate the morphology and the structure of ion-beam synthesized β-$FeSi_2$ precipitates and the defects in the Si matrix by using transmission electron microscopy (TEM) and, in a few cases, conversion electron Mössbauer spectroscopy (CEMS) or Rutherford backscattering spectrometry (RBS). We shall point out how the different process parameters affect the resulting structure and the optimum process window for light emitting application of β-$FeSi_2$. In particular, we will also show that within the optimum process window at least two different types of precipitates are obtained in separate regions: small ball-shaped precipitates in the surface region and large disc-shaped precipitates deeper in the sample. The latter are shown to display a very good interface to the Si matrix, as obtained by TEM analysis and dedicated molecular dynamics simulation. In the second part of this paper,[21] the nature and origin of the 1.54 μm PL signal obtained from our best samples will be analyzed in detail.

II. EXPERIMENTAL DETAILS

Float zone Si (100), with a *n*-type resistivity of 20 Ω cm was implanted with Fe ions at several energies in the range 250–350 keV to doses in the range $1-5\times10^{15}$ cm^{-2}. In most of the cases the substrate was maintained during implantation at a moderate temperature (between 250 and 300 °C), in order to avoid amorphization. Actually, the beam current was 0.25 $\mu A/cm^2$ to prevent unintentional beam heating. The implanted samples were subsequently annealed at temperatures between 700 and 900 °C for different times (2–20 h) in a vacuum furnace at a pressure of 2×10^{-7} torr, so that formation of iron disilicide precipitates and removal of the implantation damage were obtained. Some samples were prepared by implantation at room temperature of 340 keV Fe (dose 1.25×10^{15}, 2.5×10^{15}, and 5×10^{15} cm^{-2}) into a 700-nm-thick amorphous Si layer produced by Ge implantation at 77 K at multiple energies. These samples were then annealed at 600 °C for 1 h to achieve epitaxial regrowth of the amorphous layer, and at 800 °C for 20 h to promote the formation of the iron disilicide precipitates. Structural characterization of the samples was performed by RBS and channeling using a 2.0 MeV He^+ beam and by TEM in cross section and in plan view.

In order to analyze the local crystal symmetry or deformation of the precipitates, two sets of samples were implanted by ^{57}Fe ions to perform CEMS measurements. One set is obtained at energy of 300 keV, $T_I=300\,^{\circ}$C, and a dose of 2×10^{15} cm^{-2}, and then annealed for 20 h at 800 °C. Such a sample was analyzed before and after wet etching of the superficial layer, approximately 200 nm, where small, ball-shaped precipitates are located. Another set of samples is prepared at room temperature, with an energy of 200 keV and a dose of 5×10^{15} cm^{-2}. It was then annealed in N_2 for 18 h at 900 °C.

CEMS measurements have been performed at room temperature using a 50 mCi ^{57}Co in a Rh matrix source, which was moved by a standard constant-acceleration drive. All the spectra were taken with the angle θ between the direction of emission of the γ quantum and the surface normal equal to 0° or to 80° to check for possible texture and preferential orientation of the precipitates. The isomer shifts δ are given relative to α-Fe: a positive value of δ means that the isomeric transition has a higher energy than in α-Fe. In view of the negative calibration constant[22] this also implies a lower electron density than in α-Fe. The samples were incorporated as electrodes in a parallel plate avalanche detector.[23] The detector probes a depth d of about 400 nm with a strong attenuation for $d \geqslant 200$ nm given by the ranges of various conversion, Auger and secondary photoelectrons emitted after the nuclear resonance absorption.[24]

Wet etching of the surface region has been carried out by anodic oxidation and hydrofluoric acid (HF) removal of the oxide.[25] The oxidation is performed by a galvanostat using an ethylene glycol/H_2O(3%)/KNO_3 (0.04*M*) solution. The determination of the removed silicon layers is obtained by photometric measurement of Si concentration in the HF solution. The estimation of our etching depth by the molybdenum blue method[26] turns out to be within 10% in accuracy.

III. RESULTS

A. High-temperature implantation

The damage topology in ion-beam synthesized silicides depends on processing (implantation dose, current, and temperature). However, as a general rule, if the substrate amorphization is avoided, the implantation damage consists of small interstitial clusters.[27] These clusters evolve during postimplantation annealing and the final defect structure depends on the annealing temperature. In Fig. 1(a) the cross-section TEM analysis of as-implanted sample is shown. The region close to the surface is featureless, free of observable defects; and the dark spots located at a depth of ~ 400 nm, corresponding to the end of the range of implanted Fe, are assumed to be interstitial clusters. The micrographs after annealing at different temperatures are presented in Figs. 1(b), 1(c), and 1(d). A defect band buried at a depth close to the end of the range is always observed while the type of defect depends on the annealing temperature. In particular, interstitial clusters and small {311} stacking faults are formed after

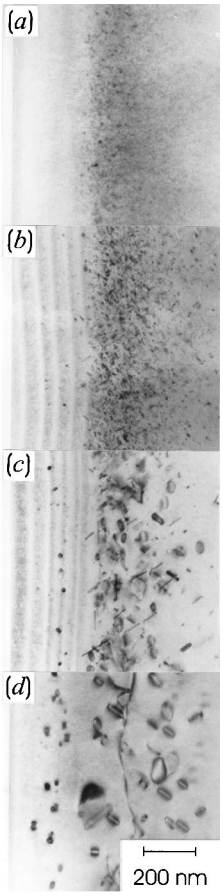

FIG. 1. Cross-section TEM images of samples implanted at 250 °C with 340 keV Fe 2.5×10^{15} cm^{-2} as grown (a), annealed at 700 °C for 3 h (b), at 800 °C for 2 h (c), and at 900 °C for 2 h (d). The surface of the samples is at the left side of the images.

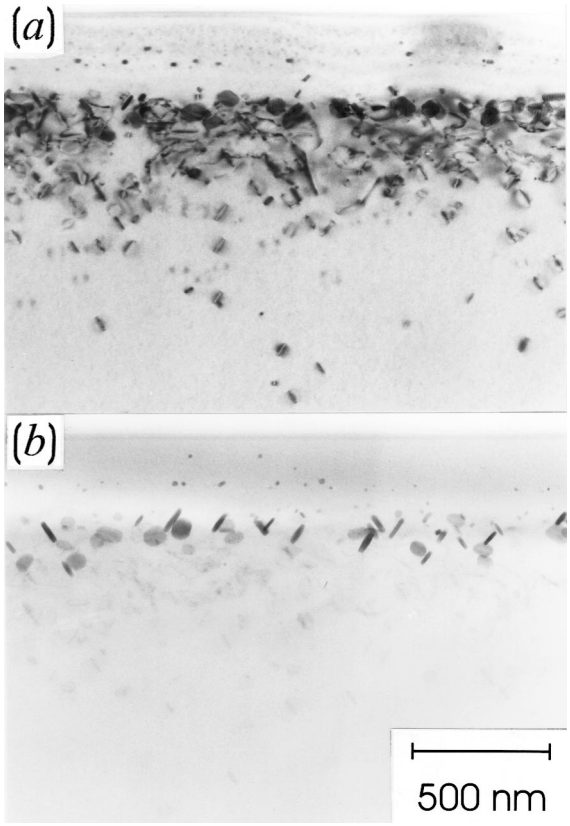

FIG. 2. Bright-field cross-section TEM micrograph of Si (100) implanted with Fe at 340 keV Fe to a dose of $2.5\times10^{15}cm^{-2}$, at $T_I=300$ °C and annealed at 800 °C for 23 h. The panel (a) is taken in two-beam configuration using the (200) Si reflection. In panel (b) the same region of the sample is analyzed far form the Bragg condition for any spots around the Si zone axis.

annealing at 700 °C [Fig. 1(b)]. By increasing the annealing temperature the interstitial clusters dissolve, and at 800 °C [Fig. 1(c)] the residual defects are represented by small dislocation loops and {311} stacking faults. At 900 °C [Fig. 1(d)] the stacking faults evolve into dislocations, originating a band of dislocation lines and loops. The density of residual defects increases with fluence, nevertheless the formation of dislocation lines is avoided if the implanted dose and the annealing temperature are kept lower than 4×10^{15} cm^{-2} and 900 °C, respectively. The comparison among PL spectra and TEM images of differently treated samples has been already reported in Figs. 1 and 2 of Ref. 28 indicating the 800 °C annealing temperature to be the optimal one. We also found out, in agreement with Ref. 29, that annealing times as long as 20 h are needed in order to get maximum PL intensity. For these reasons, in the following we limit our characterization to samples implanted at a dose lower than 3×10^{15} cm^{-2} and annealed at 800 °C, where also low dislocation-loop density in silicon is formed.

The typical cross-section TEM image of such samples is shown in Fig. 2. The first micrograph [Fig. 2(a)] was taken in bright field condition using the (220) Si reflection. Diffraction contrast allows us to detect crystallographic defects and iron silicide precipitates. A surface layer, as thick as 150–250 nm, is completely free of defects and contains a band of small spherical precipitates (top side). Deeper inside, up to 500 nm, we find a region of Si in which large disk-shaped iron disilicide precipitates are located, along with extended defects. The damage is mainly constituted by dislocation loops with a maximum concentration at a depth close to the projected ion range, and the defect density slowly decreases with depth. A few dislocation loops are still visible at 700 nm, well behind the end of range of ions. In order to enhance the visibility of precipitates, the micrograph in Fig. 2(b) was taken after tilting the sample in such a way that all the reflections around to the silicon zone axes were far from the exact Bragg positions. This configuration strongly reduces the diffraction contrast arising from defects, which can be barely distinguished in Fig. 2(b). Conversely, the iron silicide precipitates are well visible and appear dark in the micrograph. It is clearly seen that two types of precipitates, having well-defined epitaxial relationship with the substrate (as will be shown later), are present: small ones, ball shaped, with diameter of 15–30 nm in the outer layer, and large ones, disk-shaped, at a depth corresponding to the projected ion range. The latter are essentially platelets with (101) β-$FeSi_2$ preferentially oriented parallel to the Si {111} planes. Their diameter in the long side is $100\div200$ nm, whereas their thickness is 20–30 nm. This issue indicates

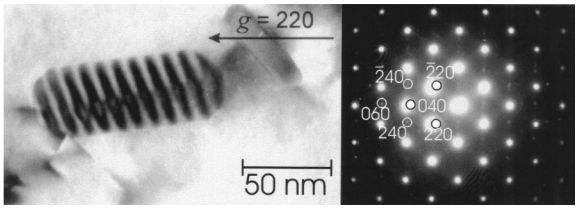

FIG. 3. High magnification of the most common disc-shaped precipitate and the corresponding diffraction pattern.

pronounced anisotropic growth since the curved borders at the rim of a plate are highly mobile,[30] whilst the interfaces along the direction perpendicular to the β-$FeSi_2$ (101) migrate only by a ledge mechanism[27].

The presence of the two types of precipitates located at a different depth can be interpreted in terms of heterogeneous nucleation of iron disilicide precipitates at the defects appeared during implantation into the Si matrix. In fact, the primary defects generated by the ion beam are point defects (interstitial and vacancies) which, at high temperatures, are mobile and do form clusters.[31,32] Because of the different momentum transfer during collisions, the vacancy clusters are closer to the surface with respect to the interstitial ones. Thus, the two types of precipitates could have originated from nucleation occurring at the vacancy clusters (ball-shaped precipitates) as well as at the interstitial clusters (disk-shaped precipitates). The larger size of the latters could also be due to an enhancement of the silicide growth rate in the presence of an excess of interstitial Si.

Selected area diffraction patterns show the existence of a well-defined epitaxial relationship between the substrate and the precipitates. The most common epitaxy is (110) β-$FeSi_2\|(1\bar{1}1)$ Si with [001] β-$FeSi_2\|$[110] Si or (101) β-$FeSi_2\|(1\bar{1}1)$ with [010] β-$FeSi_2\|$[110] Si. It is difficult to distinguish between the two because of the large similarity between the b and c lattice constants of the β-$FeSi_2$. The (110), or (101) planes are, with the same probability, parallel to the four equivalent {111} Si planes. Therefore, the projected image of a large precipitate will be different depending on the spatial orientation of the precipitate. In Fig. 2(b), for example, the rodlike precipitates are platelets with (110) or (101) β-$FeSi_2$ parallel to the two (111) Si planes perpendicular to the image. The elliptical shapes correspond, on the contrary, to the other two (111) planes. The precipitates exhibit Moirè fringes (Figs. 3, 4, and 5) due to the interference between Si and β-$FeSi_2$ crystal planes of different spacing. In the general case, where the spacing of the relevant lattice planes are d_1 (Si) and d_2 (β-$FeSi_2$) and the angle between them is φ, the Moirè spacing D is given by

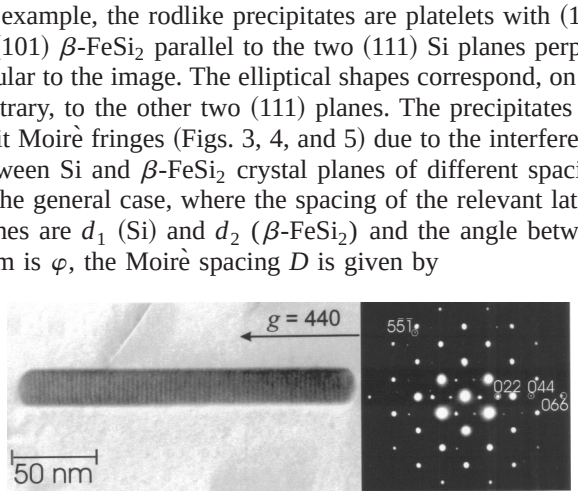

FIG. 4. High magnification of a disc-shaped precipitate and the corresponding diffraction pattern.

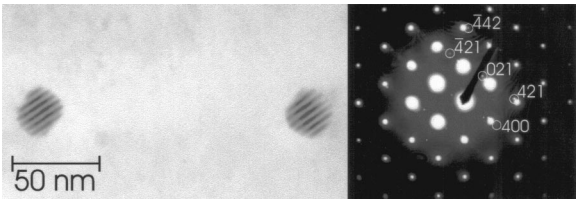

FIG. 5. High magnification of a small ball-shaped precipitate and the corresponding diffraction pattern.

$$D=\frac{d_1 d_2}{\sqrt{d_1^2+d_2^2-2d_1 d_2\cos\varphi}}.$$

The angle Θ of the Moirè pattern relative to the planes of spacing d_1 is given by

$$\Theta=\frac{d_1\sin\varphi}{\sqrt{d_1^2+d_2^2-2d_1 d_2\cos\varphi}}.$$

We measured the Moirè fringes spacing with an accuracy $\Delta D/D=2\%$ and the angle Θ with an error $\Delta\Theta=3°$, from which the interplanar distance d_2 can be calculated to a good accuracy.

The micrographs of Figs. 3, 4, and 5 are taken in two-beam conditions using the (220) silicon reflection under kinematical contrast. They show the magnified structure of some large (Figs. 3 and 4) and small (Fig. 5) precipitates. The weak extra spots superimposed on the pattern of the (110) Si pole in the diffraction of Fig. 3 derive from the precipitate shown on the left. The fundamental pattern due to the silicide has been recognized and indexed although double diffractions complicate the pattern. The Moirè fringes in the precipitate of Fig. 3 arise from the interference of the beams diffracted by the (220) Si and (040) β-$FeSi_2$. Using the measured fringe spacing $D=8.32$ nm and $\Theta=14°$ [with respect to the (110) Si] we have determined $d_2=0.1963$ nm and $\varphi=0.3°$. In evaluating the error on the interplanar distance we calculate d_2 vs D and Θ within the experimental indetermination and we found that $\Delta d_2/d_2\sim 0.2\%$. By considering the bulk lattice parameters of β-$FeSi_2$, the expected interplanar distance is 0.1948 and 0.1958 nm (0.5% difference) for the (004) and (040) set of planes, respectively. Thus, the interplanar distance calculated by the analysis of the Moirè fringes is very close, within the error, to that one of (040) β-$FeSi_2$, and this suggests that in precipitates the epitaxy consists mainly of (101) β-$FeSi_2\|$(111) Si. Most of the large precipitates exhibit this type of epitaxy (in agreement with literature data,[1,2]) with the exception of a few grains (about 1 over 20) in which the (011) β-$FeSi_2$ are parallel to the (110) Si planes with [211] β-$FeSi_2\|$[110] Si (Fig. 4). The fundamental pattern due to the silicide has been recognized and indexed in the diffraction shown on the rigth side of the figure. The Moirè fringes, deriving from the interference of (066) β-$FeSi_2$ with (440) Si planes, have a spacing of 2.54 nm and are parallel to the (440) Si planes. Analysis of the fringes indicates that the (066) β-$FeSi_2$ are parallel to the (440) Si planes and that the (066) distance is 0.0926 ± 0.0001 *nm* to be compared with 0.0921 nm expected of

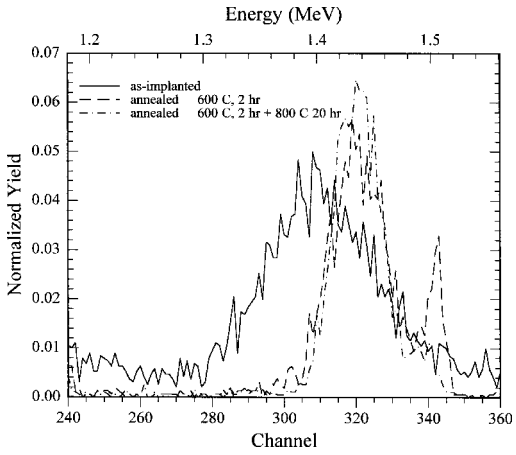

FIG. 6. Fe concentration profile in as-implanted amorphous Si (solid line), after annealing at 600 °C for 2 h (dashed line) and 800 °C for 20 h (dot-dashed line) as detected by RBS of 2.0 MeV He^+ beam.

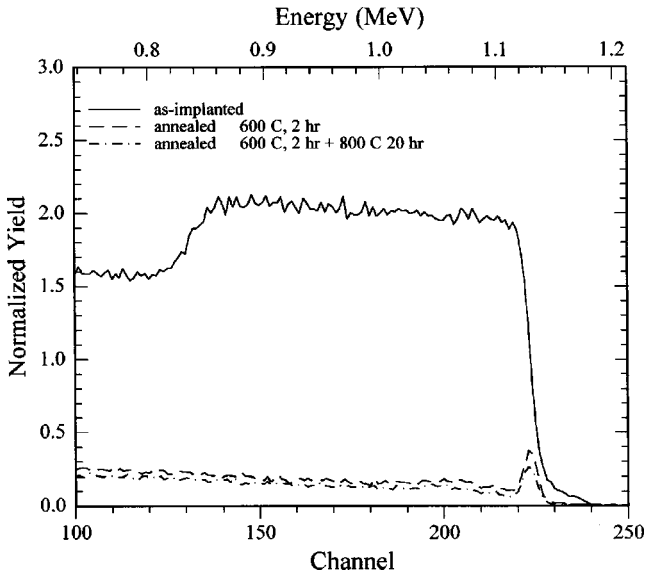

FIG. 7. Channeling RBS spectra of the sample in Fig. 6 for a 2.0 MeV He^+ beam.

bulk β-$FeSi_2$. For each one of the large precipitates that we considered, the Moirè parameters allowed for an accurate evaluation of the interplanar distance in the β-$FeSi_2$ platelets, and the obtained values match (within 0.5%) those expected of bulk β-$FeSi_2$. We deduce that the large precipitates are mostly relaxed.

The diffraction pattern of Fig. 5, which corresponds to nearly half of the small spherical grains, shows that such particles are β-$FeSi_2$ precipitates having the following epitaxial relationship: (100) β-$FeSi_2\|$(111) Si with [012] β-$FeSi_2\|$[110] Si. In particular, the (400), (421), and (44 2) precipitate spots are very close to the (111), (220), and (004) silicon spots and do produce Moirè fringes. By a detailed analysis of the fringe spacing and angles we estimated the interplanar distances of those β-$FeSi_2$ planes, obtaining the following values: 0.259 ± 0.002,0.201 ± 0.002, and 0.136 ± 0.004 nm, respectively. The interplanar distances obtained by the analysis on small precipitates differ considerably from the ones calculated by using the bulk lattice parameters: 0.247 nm, 0.201 nm, and 0.142 nm for the (400), (421), and (44 2) β-$FeSi_2$ planes, respectively. Such an issue suggests that the small spherical precipitates are heavily strained, with orthorhombic lattice parameters corresponding to $a = 1.036$ nm, $b = 0.736$ nm, and $c = 0.740$ nm, which means an increase in a by 4.8% and a decrease in b and c by 5.5% with respect to the bulk material.

B. Room-temperature implantation

The RBS spectra relative to the as-implanted (with 5×10^{15} cm^{-2} at RT into a 700-nm-thick amorphous silicon) and annealed samples are shown in Figs. 6 and 7, respectively. The concentration profile of the as-implanted Fe is gaussian with a maximum concentration of 2.5×10^{20} cm^{-3} at a depth of $\sim$250 nm. The amorphous Si completely recrystallizes after annealing at 600 °C (Fig. 7), and the Fe distribution is shifted toward the surface with a maximum concentration of 3.5×10^{20} cm^{-3} at a depth of $\sim$120 nm (Fig. 6). A small amount of Fe ($\sim$10% of the implanted dose) is segregated at the sample surface. The modifications of the Fe profile are prototypical for a process in which segregation of the impurities occurs at the moving amorphous-crystalline interface during the solid-phase epitaxial regrowth of Si. In fact, it is known that the solid solubility of several transition metals in crystalline Si is lower than that in amorphous Si.[33] Because of this difference, impurity accumulates in the amorphous layer as the amorphous-cystalline interface moves toward the surface during epitaxial crystallization. When the impurity concentration in the amorphous layer exceeds the amorphous solid solubility, precipitation of the impurity occurs. The resulting impurity concentration profile after annealing cannot be fitted as a simple diffusion process driven by the concentration gradient. TEM analysis, presented in Fig. 8, shows that the Fe retained inside the layer consists of very small iron silicide clusters. The Fe peak at the sample surface disappears after the successive annealing at 800 °C, because it is gettered into the growing iron disilicide precipitates. The crys-

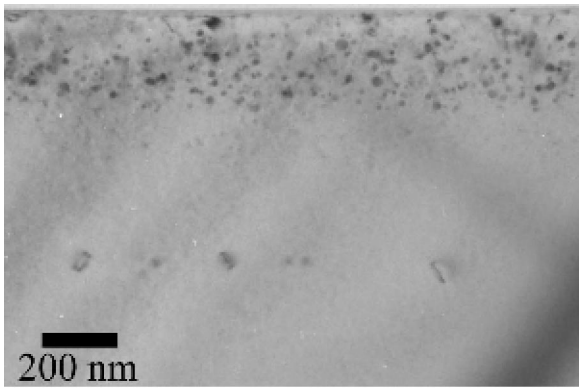

FIG. 8. Cross-section bright-field image of the Fe-implanted amorphous silicon after annealing at 600 °C for 2 h and then at 800 °C for 23 h.

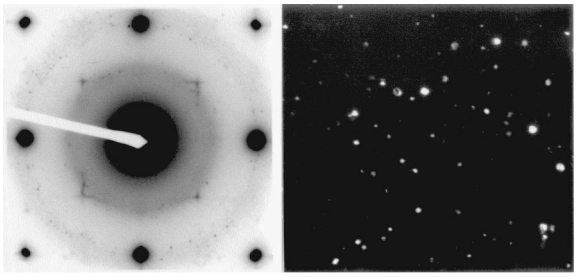

FIG. 9. Diffraction pattern along the [100] Si pole of the Fe implanted amorphous Si after annealing at 600 °C for 2 h and then 800 °C for 20 h and dark field plan view image using the beam diffracted inside the ring.

talline quality of regrown Si is excellent, as testified by the reduction of the backscattering yield. The ratio of the channeled to the random yield (Fig. 7) just below the surface peak is 4%, representative of a defect-free Si single crystal. The very good quality of the sample is also confirmed by cross-section TEM analysis displayed in Fig. 8. Only spherical precipitates with a diameter of ~ 20 nm are visible and the layer is completely free of defects. Therefore, the crystalline quality is better with respect to samples implanted at high temperature (Fig. 2). The reason for this property relays on the processing (a superior crystalline quality is generally achieved by solid-phase epitaxy of amorphous Si) and on the absence of the strain field induced by the coherence between the silicon and the precipitates. The latter ones are in fact randomly oriented, as it is clearly seen from the diffraction pattern along the [110] Si pole shown in Fig. 9. Rings belonging to β-$FeSi_2$ are evident, and the dark field images constructed on the different rings confirm a mainly random distribution of the precipitates. Still, these very nice samples do not provide any PL signal suggesting that a good quality β-$FeSi_2$ structure in nanometric precipitates is not a sufficient issue to get light out of them. More indications will come from CEMS measurements and molecular dynamics simulations.

C. CEMS measurements

The CEMS spectra, presented in Fig. 10, correspond to different samples: a reference polycrystalline β-$FeSi_2$, and two samples obtained at room- and high-temperature implantation. The Mössbauer parameters, isomer shifts δ, linewidth Γ, quadrupole splitting Δ, and area ratio A_2/A_1, between the high- and low-energy quadrupole components, as well as the spectral fraction are summarized in Table I.

The polycrystalline sample reveals CEMS parameters in good agreement with those observed in epitaxial layers of β-$FeSi_2$.[34]

The spectra of sample implanted at room temperature are consistent only to fully relaxed β-$FeSi_2$ precipitates. The observed angular dependence of the ratio A_2/A_1 indicates partial orientation of the precipitates.

The situation is more complicated for the sample implanted at high temperature. The smaller effect (total area/background) can be fully attributed to the lower dose and the higher implantation energy. A fit with only two quadrupole

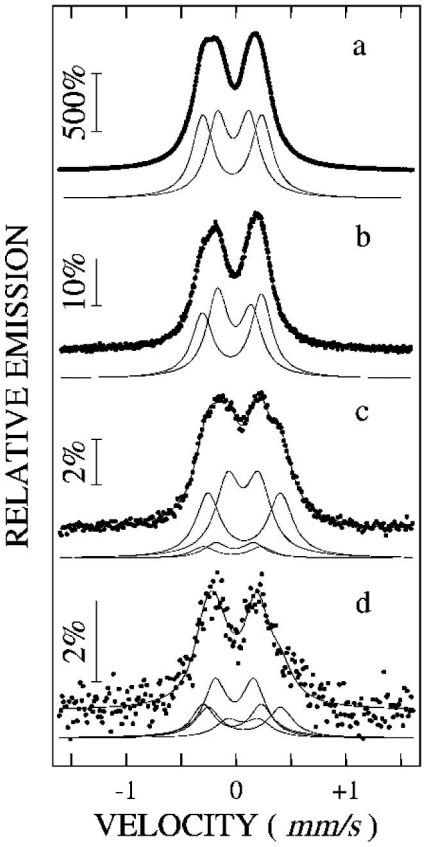

FIG. 10. CEMS spectra of different samples: β-$FeSi_2$ polycristalline sample (a); sample implanted at room temperature (b); sample implanted at high temperature before (c) and after (d) etching. The spectra were taken with the angle Θ between the direction of emission of the γ quantum and the surface normal equal to 0.

doublets was found to be inadequate. A fit with four quadrupole doublets, two of them related to the relaxed β-$FeSi_2$ (Fe_I and Fe_{II}) and the other two to a strained β-$FeSi_2$ phase (Fe_{III} and Fe_{IV}), as revealed by TEM, gives a reasonable χ^2 (1.09). As expected, the population fraction of Fe_I and Fe_{II} are identical, within the experimental error.

By taking into account the TEM results, indicating that the relaxed β-$FeSi_2$ precipitates are located at a depth far larger than 250 nm, the spectral areas of Fe_I and Fe_{II} are strongly attenuated, while those related to Fe_{III} and Fe_{IV}, probably originated from strained spherical precipitates in the surface region, are less attenuated. A confirmation that such precipitates are located mainly in a region closer to the surface is provided by the reduction of the intensity of the Fe_{III} and Fe_{IV} lines after chemical etching [Fig. 10(d)]. Due to the presence of several epitaxial relationships with the crystalline matrix (and of the corresponding strain value), as indicated by the TEM analysis, it is impossible to analyze the data with more complex fits, even by taking into account the possible occurrence of metastable phases.[35] Actually, the shoulder observed at lower energy (positive velocity) could be related to the presence of the α-$FeSi_2$. Still, the difficulty in taking into account the presence of this phase is due to the complexity of its CEMS spectrum.[35–37]

TABLE I. Mössbauer parameters of Fe_I and Fe_{II} in β-$FeSi_2$ and for the investigated samples (δ relative to α-Fe at room temperature). The error bars on the last digit are reported in parentheses.

Sample	Site	δ(mm/s)	Γ(mm/s)	Δ(mm/s)	Specral area %	Ratio $A2/A1$
Pollycrystalline	Fe_I	0.079(8)	0.23(2)	0.537(8)	51(1)	1
	Fe_{II}	0.088(8)	0.23(2)	0.288(8)	49(1)	1
Implanted at	Fe_I	0.077(8)	0.23(1)	0.54(1)	50(1)	1.32(5)
room temperature	Fe_{II}	0.098(5)	0.23(1)	0.31(1)	50(1)	0.77(5)
Implanted at	Fe_I	0.080(8)	0.25(1)	0.53(1)	7(1)	1.0
high temperature	Fe_{II}	0.099(5)	0.25(1)	0.35(1)	8(1)	1.0
	Fe_{III}	0.19(5)	0.27(1)	0.66(1)	39(1)	1.0
	Fe_{VI}	0.18(5)	0.27(1)	0.28(1)	46(1)	1.0
Implanted at	Fe_I	0.080(5)	0.25(1)	0.53(1)	24(4)	1.0
high temperature	Fe_{II}	0.099(5)	0.25(1)	0.35(1)	39(5)	1.0
with etching of 200 nm	Fe_{III}	0.19(5)	0.27(1)	0.66(1)	24(1)	1.0
	Fe_{VI}	0.18(5)	0.27(1)	0.28(1)	13(1)	1.0

From these results we can conclude that the small spherical precipitates randomly oriented in a Si recrystallized matrix (RT implantation) are fully relaxed β-$FeSi_2$, as the large disk-shaped precipitates located between 250 and 500 nm in the samples implanted at high temperature, whereas the small spherical precipitates in the surface region of the latter samples are different in strain and possibly in phase too.

D. Molecular dynamics simulation

In order to understand the reasons why our large precipitates display a disk-shaped morphology with big and flat interface β-$FeSi_2$(110) or (101)$\|$Si(111), we have to consider the crystallographic origin of the orthorhombic structure. In Fig. 11 the correspondence between four tetragonal cells (the ones giving rise to the orthorhombic conventional cell after the Jahn-Teller distortion) and eight cubic CaF_2 cells of the parent γ-$FeSi_2$ phase is shown. We note that β-$FeSi_2$ (110) or (101) coincides with γ-$FeSi_2$ (111) and that β-$FeSi_2$ (100) corresponds to γ-$FeSi_2$ (100), after a 45° rotation along the vertical $\langle 100 \rangle$ axis. Now, γ-$FeSi_2$ has only Si sites corresponding to the Si sites of silicon in the (111) plane, whereas the (100) plane of γ-$FeSi_2$ displays a double Si density with respect to Si (100). Therefore, we expect β-$FeSi_2$(110) or (101)$\|$Si(111) to display a good correspondence of the silicon atoms in the β-$FeSi_2$ plane to the ones in Si diamond, but for the limited variations in the atomic positions and the lattice parameters provided by the Jahn-Teller distortion. In Fig. 12 such a top view of interfaces is reported, displaying the positions of the β-$FeSi_2$ silicon atoms (open circles) and the positions of the Si-diamond atoms (full circles), when the relevant lattice mismatch of the formers (Fig. 12, bottom side) is accommodated by strain. Actually, the elastic energy provided by setting β-$FeSi_2$ (101) or (110) on top of Si(111) in a coherent growth is the largest one among most of the possible epitaxial relationships, both calculated by tight-binding potentials with a full molecular dynamics relaxation[38] and obtained by *ab initio* optimization.[6] Since our TEM analysis indicates that the β-$FeSi_2$ platelets are fully relaxed in bulk structure, it is a meaningful item to understand how the silicon matrix [half of the bulk modulus of β-$FeSi_2$ (Ref. 9)] rearranges near the β-$FeSi_2$ (101) or (110)$\|$Si(111) interface in order to accommodate the interface stress, by taking full advantage of the good matching of the atomic positions.

To this end we simulated by classical molecular dynamics with a Tersoff potential[39] the structural relaxation of a silicon slab on top of two β-$FeSi_2$ (110) silicon planes, which are kept fixed in their bulk positions. The latter ones correspond to nine surface cells along β-$FeSi_2$ $\langle 110 \rangle$ and 50 cells along β-$FeSi_2$ $\langle 001 \rangle$ whereas the Si slab, 28 atomic planes on top of the two fixed Si planes (4.78 nm all together) with a free surface, corresponds to 51 cells along Si $\langle 110 \rangle$ (39.17 nm)

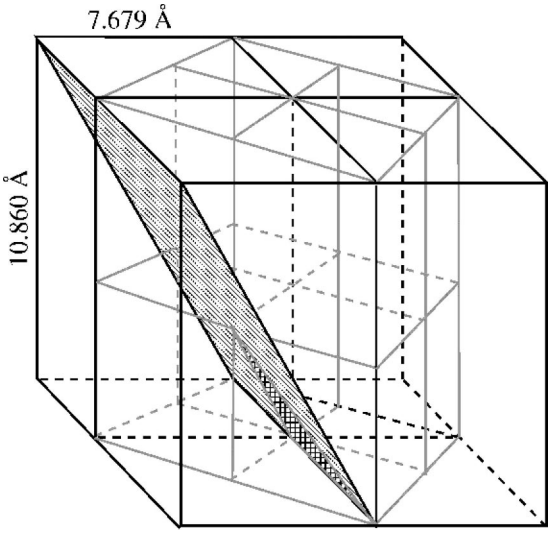

FIG. 11. Correspondence between four "tetragonal" β-$FeSi_2$ conventional cells before the Jahn-Teller distortion (black lines) and eight cubic γ-$FeSi_2$ cells (gray lines). The (110) or (101) plane of former superimposes to the (111) plane of the latter (shaded areas). β-$FeSi_2$ (100) corresponds to γ-$FeSi_2$ (100), but for an in-plane rotation by 45°.

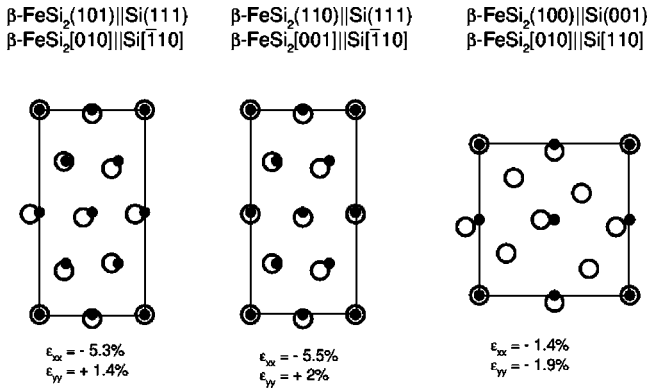

FIG. 12. Top view of the atomic matching at β-$FeSi_2\|Si$ interfaces. The projection of one orthorhombic cell of iron disilicide is shown, where the open and the solid circles correspond to Si atoms in β-$FeSi_2$ and in the silicon matrix, respectively. The strains in the plane (ϵ) are also reported.

and 17 cells along Si $\langle 112 \rangle$ (11.31 nm), giving rise to a different Si areal density and to a negligible lattice mismatch (some 10^{-3}%).

Starting by the initial conditions where the structural mismatch is uniformly distributed along the interface cell [Fig. 13(a)], we performed a simulated annealing for 104 172 Si atoms by rising the temperature to 400 K for 0.3 ns, and quenching it to 0 K for 10 ps. Figure 13(b) presents the corresponding top view of the interface, which displays large coherent areas separated by narrow regions where the lattice misfit is accommodated. Such regions can be classified as *A* and *B* types [Fig. 13(c)], corresponding to two stacking fault

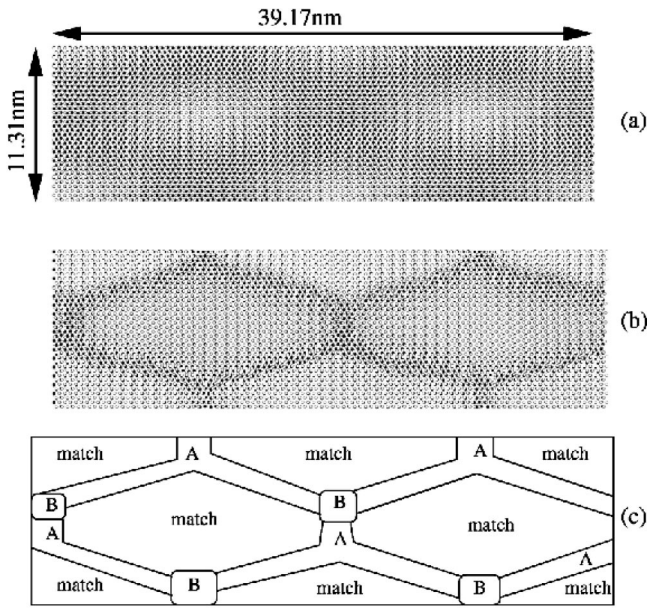

FIG. 13. Top view of the β-$FeSi_2$ (110)$\|$Si (111) interface (as thick as two atomic layers), taken from the β-$FeSi_2$ side, before (a) and after (b) atomic relaxation. Open circles correspond to the fixed Si atoms in β-$FeSi_2$, solid circles are the simulated Si atoms of the silicon matrix. A map of the regions related to the different mismatch conditions is reported in panel (c) (see text).

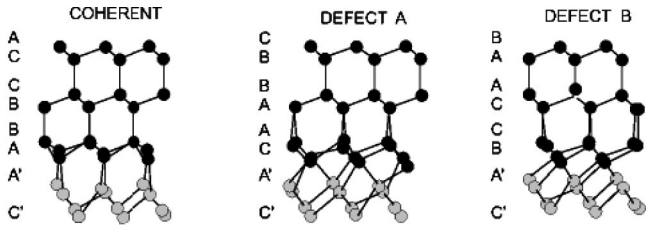

FIG. 14. Cross section of the β-$FeSi_2$ (110)$\|$Si (111) interface (as thick as two atomic layers), corresponding to matched (coherent), *A* and *B* defected areas, as shown in Fig. 13.

configurations for diamond silicon, named SFA and SFB, as displayed in a cross section view in Fig. 14. Here it is seen that the coherent region corresponds to the usual $AABBCCAA$ stacking ($C'A'$ label the β-$FeSi_2$ planes), whereas a staking fault $C'A'CAABB\ldots$ corresponds to SFA and a staking fault $C'A'BCCAA\ldots$ corresponds to SFB.

Three nice results are obtained by such a rearrangement. First, the elastic energy by bond stretching at the interface is minimized; second, no dangling bonds are produced at the interface (that is not likely to be the case for the relaxed ball-shaped precipitates in the recrystallized matrix), since the SFA and SFB regions display silicon overcoordination (Fig. 14); third, the interface is mesoscopically flat (as it appears in the TEM cross sections), but for a slight deformation of the Si slab at the SFA and SFB regions. The latter issue is barely visible in Fig. 15. There a full cross section including two SFA regions is reported, along with the indication of the Burger circles around them, indicating the misfit dislocations at the interface.

IV. CONCLUSIONS

In this paper we report an extensive investigation on morphological and structural properties of $FeSi_2$ precipitates in silicon, produced by IBS process.

The samples obtained by implantation at RT in amorphous silicon give rise to the best structural properties. With this process high-quality ball-shaped ($\sim$20 nm in diameter) relaxed β-$FeSi_2$ precipitates randomly oriented in a defect-

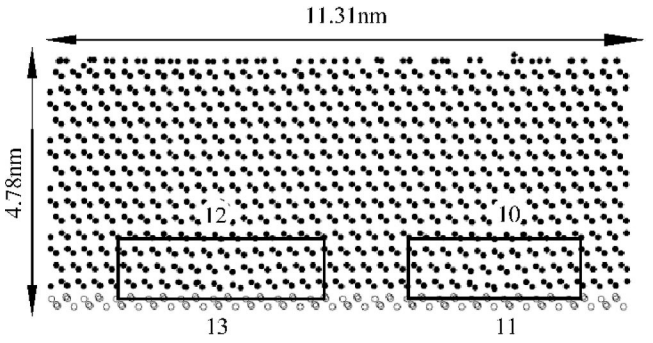

FIG. 15. Cross section of the full simulation cell including two SFA regions, corresponding to a vertical line in Fig. 13. The Burger circles around the SFA region indicate that one atomic plane is there missing. Open and solid circles stand for Si atoms in β-$FeSi_2$ and the silicon matrix, respectively.

free Si matrix are generated during the epitaxial regrowth of the amorphous Si. In spite of the excellent crystalline quality of both precipitates and Si matrix, no PL signal was detected in a preliminary characterization of the samples.

Many authors[10–13,28,29] have reported light emission from β-$FeSi_2$ nanocrystals enbedded in silicon. In order to clarify the correlation between morphology and structure of both Si matrix and $FeSi_2$ precipitates from one side and the possibility to observe a radiative recombination into the latters on the other side, we have extended our investigation to a set of samples that are known[13,28] to provide a PL signal. In these samples two populations of precipitates different in microstructure and performance are unavoidably obtained. Fortunately, such populations are spatially far apart and can be characterized separately. Precipitates close to the Si surface are small ($\sim$20 nm), ball-shaped, and strained by the epitaxy inside a defect-free matrix. The ones close to the end of range of the implanted ion are fully relaxed, disc-shaped (as large as $\sim$200 nm), and surrounded by the defects due to the accommodation of the lattice mismatch. Most of the latter ones exhibit the epitaxial relationship β-$FeSi_2$ (101) or (110)$\|$Si (111) and despite the presence of some defects, they originate a PL signal, as it is suggested in Refs. 21 and 13.

We believe that the best morphology turns out to be the one of the disk-shaped precipitates, since the large interfacial area β-$FeSi_2$ (101) or (110)$\|$Si (111) luckily displays a perfect atomic matching. Somehow a similar, still not so efficient, situation is provided by β-$FeSi_2$ (100)$\|$Si (100), as it is obtained by MBE reactive epitaxy of $FeSi_2$ microcrystals on Si (100) performed by the authors of Refs. 11 and 29, where PL and electroluminescence signals are actually observed.

The reason why both the small spherical precipitates obtained by RT implantation or the strained ones at the surface layers of the high-temperature implanted samples (here the presence of metallic α-$FeSi_2$ is not excluded) do not contribute to PL signal is probably the presence of dangling bonds at the interfaces, acting as nonradiative recombination centers. This issue will be also addressed in the second part of this paper.

ACKNOWLEDGMENTS

This work was partially supported by Cofinanziamento 40% 1998 of the Italian Ministry of University and Research (Grant No. 9802154837).

[1] H. Lange, Phys. Status Solidi B **201**, 3 (1997).
[2] *Semiconducting Silicides*, edited by V. E. Borisenko (Springer, Berlin, 2000).
[3] A.B. Filonov, D.B. Migas, V.L. Shaposhnikov, N.N. Dorozhkin, G.V. Petrov, V.E. Borisenko, W. Henrion, and H. Lange, J. Appl. Phys. **79**, 7708 (1996).
[4] A.B. Filonov, D.B. Migas, V.L. Shaposhnikov, V.E. Borisenko, W. Henrion, M. Rebien, P. Stauss, H. Lange, and G. Behr, J. Appl. Phys. **83**, 4410 (1998).
[5] D.B. Migas, L. Miglio, W. Henrion, M. Rebien, F. Marabelli, B.A. Cook, V.L. Shaposhnikov, and V.E. Borisenko, Phys. Rev. B **64**, 075208 (2001).
[6] D.B. Migas and L. Miglio, Phys. Rev. B **62**, 11 063 (2000).
[7] S.J. Clark, H.M. Al-Allak, S. Brand, and R.A. Abram, Phys. Rev. B **58**, 10 389 (1998).
[8] L. Miglio, V. Meregalli, and O. Jepsen, Appl. Phys. Lett. **75**, 385 (1999).
[9] E.G. Moroni, W. Wolf, J. Hafner, and R. Podloucky, Phys. Rev. B **59**, 12 860 (1999).
[10] D.N. Leong, M.A. Harry, K.J. Reeson, and K.P. Homewood, Nature (London) **387**, 686 (1997).
[11] T. Suemasu, Y. Negishi, K. Takakura, and F. Hasegawa, Jpn. J. Appl. Phys., Part 2 **39**, L1013 (2000).
[12] T.D. Hunt, B.J. Scaly, K.J. Reeson, R.M. Gwilliam, K.P. Homewood, R.J. Wilson, C.D. Meekison, and G.R. Booker, Nucl. Instrum. Methods Phys. Res. B **74**, 60 (1993).
[13] C. Spinella, S. Coffa, C. Bongiorno, S. Pannitteri, and M.G. Grimaldi, Appl. Phys. Lett. **76**, 173 (2000).
[14] P.Y. Dusausoy, J. Protas, R. Wandji, and B. Roques, Acta Crystallogr., Sect. B: Struct. Crystallogr. Cryst. Chem. **27**, 1209 (1971).
[15] H. Sirringhaus, N. Onda, E. Muller-Gubler, R. Stalder, and H. von Känel, Phys. Rev. B **47**, 10 567 (1993).
[16] H. Moritz, B. Rösen, S. Popovic, A. Rizzi, and H. Lüth, J. Vac. Sci. Technol. B **10**, 1704 (1992).
[17] H. von Känel, K.A. Mäder, E. Müller, N. Onda, and H. Sirringhaus, Phys. Rev. B **45**, 13 807 (1992).
[18] R.L. Maltez, L. Amaral, M. Behar, A. Vantomme, G. Langouche, and X.W. Lin, Phys. Rev. B **54**, 11 659 (1996).
[19] X.W. Lin, M. Behar, J. Desimoni, H. Bernas, J. Washburn, and Z. Liliental-Weber, Appl. Phys. Lett. **63**, 105 (1993).
[20] J. Desimoni, H. Bernas, M. Behar, X.W. Lin, J. Washburn, and Z. Liliental-Weber, Appl. Phys. Lett. **62**, 306 (1993).
[21] L. Martinelli, E. Grilli, D. B. Migas, L. Miglio, F. Marebelli, C. Soci, M. Geddo, M. G. Grimaldi, and C. Spinella, Phys. Rev. B **66**, 085320 (2002).
[22] O. Eriksson and A. Svane, J. Phys.: Condens. Matter **1**, 1589 (1989).
[23] G. Weyer, Mössbauer Effect Methodology **10**, 301 (1976).
[24] D. Liljequist, T. Ekdahl, and U. Bäverstam, Nucl. Instrum. Methods **155**, 529 (1978).
[25] H.D. Barber, H.B. Lo, and J.E. Jones, J. Electrochem. Soc. **146**, 1873 (1999).
[26] F.D. Smedt, G. Stevens, S.D. Gendt, I. Cornelissen, S. Arnauts, M. Meuris, M.M. Heyns, and C. Vinckier, J. Electrochem. Soc. **123**, 1404 (1976).
[27] S. Mantl, J. Phys. D **31**, 1 (1998).
[28] M.G. Grimaldi, S. Coffa, C. Spinella, F. Marabelli, M. Galli, L. Miglio, and V. Meregalli, J. Lumin. **80**, 467 (1999).
[29] T. Suemasu, Y. Iikura, K. Takakura, and F. Hasegawa, J. Lumin. **87-89**, 528 (2000).
[30] S. Mantl, Mater. Sci. Rep. **8**, 1 (1992).
[31] J.L. Benton, S. Libertino, P. Kringhoj, D.J. Poate, and S. Coffa, J. Appl. Phys. **82**, 120 (1997).

[32] D.C. Schmidt, B.G. Svensson, S. Godey, E. Ntsoenzok, J.F. Barbot, and C. Blanchard, Nucl. Instrum. Methods Phys. Res. B **147**, 127 (1999).
[33] J.S. Custer, M.O. Thompson, D.J. Eaglesham, D.C. Jacobson, and J.M. Poate, J. Mater. Res. **8**, 820 (1993).
[34] M. Fanciulli, C. Rosenblad, G. Weyer, V. Svane, N.E. Christensen, and H. von Känel, Phys. Rev. Lett. **75**, 1642 (1995).
[35] M. Fanciulli, C. Rosenblad, G. Weyer, H. von Känel, and N. Onda, Thin Solid Films **275**, 8 (1996).
[36] C. Blaauw, F. van der Wounde, and G.A. Sawatzky, J. Phys. C **6**, 2371 (1973).
[37] O. Helgason and T.I. Sigfüsson, Hyperfine Interact. **45**, 415 (1989).
[38] M. Gemelli and L. Miglio, Thin Solid Films **380**, 282 (2000).
[39] J. Tersoff, Phys. Rev. B **39**, 5566 (1989).